Available online at www.sciencedirect.com

ScienceDirect

journal homepage: www.elsevier.com/locate/he

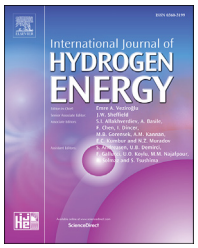

Palladium nanoparticles grown on β-Mo_2C nanotubes as dual functional electrocatalysts for both oxygen reduction reaction and hydrogen evolution reaction

Tingzhen Li [a,b], *Zhenghua Tang* [a,c,*], *Kai Wang* [a], *Wen Wu* [a], *Shaowei Chen* [a,d], *Changhong Wang* [b,**]

[a] *Guangzhou Key Laboratory for Surface Chemistry of Energy Materials, New Energy Research Institute, School of Environment and Energy, South China University of Technology, Guangzhou Higher Education Mega Centre, Guangzhou, 510006, PR China*

[b] *School of Materials and Energy, Guangdong University of Technology, Guangzhou, 510006, PR China*

[c] *Guangdong Provincial Key Laboratory of Atmospheric Environment and Pollution Control, Guangdong Provincial Engineering and Technology Research Center for Environmental Risk Prevention and Emergency Disposal, South China University of Technology, Guangzhou Higher Education Mega Centre, Guangzhou, 510006, PR China*

[d] *Department of Chemistry and Biochemistry, University of California, 1156 High Street, Santa Cruz, CA 95064, United States*

ARTICLE INFO

Article history:
Received 25 November 2017
Received in revised form
8 January 2018
Accepted 18 January 2018
Available online 14 February 2018

Keywords:
Palladium nanoparticles
Mo_2C nanotubes
Dual functional electrocatalysts
Oxygen reduction reaction
Hydrogen evolution reaction

ABSTRACT

Developing efficient dual functional electrocatalysts for both oxygen reduction reaction (ORR) and hydrogen evolution reaction (HER) is critical for boosting the performance of fuel cells and metal air batteries, as well as production of clean and sustainable energy source. Herein, Pd nanoparticles grown on Mo_2C nanotubes were prepared as dual functional electrocatalysts for both ORR and HER. A series of samples with different Pd loadings were fabricated, while the morphology and the structural features were well examined by transmission electron microscopy (TEM), X-ray diffraction (XRD) and X-ray photoelectron spectroscopy (XPS). Interestingly, both the ORR activity and HER activity first increased then decreased with the increasing of Pd loading, and the sample of Mo_2C-Pd-9% exhibited the best performance among the series, superior than commercial Pd/C in both ORR and HER tests. Furthermore it also exhibited markedly higher long-term stability than Pd/C for both electrocatalytic reactions. The results may shed light on rational design of novel bi-functional electrocatalysts in the renewable energy field.

* *Corresponding author*. Guangzhou Key Laboratory for Surface Chemistry of Energy Materials, New Energy Research Institute, School of Environment and Energy, South China University of Technology, Guangzhou Higher Education Mega Centre, Guangzhou, 510006, PR China.

** *Corresponding author*.

E-mail addresses: zhht@scut.edu.cn (Z. Tang), wangchh@gdut.edu.cn (C. Wang).

https://doi.org/10.1016/j.ijhydene.2018.01.107

Introduction

The global energy crisis and extensive environmental pollution caused by the heavily reliance of fossil fuels can be significantly mitigated by the rapidly developing green and sustainable energy technologies including water splitting, fuel cells and metal-air batteries [1–4]. Oxygen reduction reaction (ORR) plays a key role in fuel cells and metal-air batteries, while hydrogen evolution reaction (HER) is critical for production of clean energy [5–8]. Currently, Pt based nanomaterials have been widely considered as the state-of-art electrocatalysts for both ORR and HER thanks to their low overpotentials and large current densities [9–11]. Nevertheless, the low abundance and high costs of Pt significantly hindered their large-scale commercialization. Therefore, developing cost-effective, highly active and durable catalysts for ORR and HER as alternative of Pt is crucial and highly desirable [7,11–17].

Compared with Pt, palladium has demonstrated as a promising candidate to replace Pt due to its much lower costs and satisfactory catalytic activities in electrochemical reactions [18–22]. For instance, a series of Pd nanoparticles with various size exhibited effective catalytic activity toward ORR, and Zhou et al. successfully established the size effects [23]. Xia group synthesized 5–6 nm Pd nanocrystals with different shapes, and surface-structure-dependent ORR activities were observed [24]. By employing a top-down strategy, Xu group created a multisite HER catalyst on nano-Pd surface, where the water dissociation and hydrogen formation were balanced to achieve the highest efficiency for HER in alkaline media [25]. Recently, Liu et al. developed a facile approach to prepare Pd nanoparticle assemblies with porous structure for both HER and ORR, of which the Tafel slope was 30 mV dec^{-1} and the overpotential was 80 mV at 100 mA cm^{-2} for HER, while the half-wave potential and onset potential was 0.84 V and 0.93 V for ORR, respectively [26].

Nevertheless, when employing palladium nanoparticles alone to catalyze electrochemical reactions, the catalysts still suffer from low chemical susceptibility, as palladium nanoparticles would aggregate or decompose during the catalytic process. A matrix or support to integrate palladium nanoparticle as an intact hybrid catalyst is highly desirable [27]. In addition, such matrix or support would be easily accessible and the introduction of additional electrocatalytic activity is desired. Mo_2C nanotubes can be a great choice based on the following reasons: First of all, Mo_2C nanotubes can be fabricated under mild conditions in large scale with low costs; Secondly, previous studies have shown that Mo_2C nanotubes and/or their analogues exhibited a remarkable electrocatalytic performance toward HER [28–30]. Lastly and most importantly, through rational design, palladium nanoparticles can be grown on the surface of the Mo_2C nanotubes to form an integral composite, and enhancement of electrocatalytic performance via the synergistic effect is expected.

Herein, we report a facile approach to prepare palladium nanoparticles grown Mo_2C nanotubes. The as-prepared integral composite exhibited effective catalytic activities toward both ORR and HER. Among a series of samples tested, Mo_2C–Pd-9% demonstrated the best performance toward both ORR and HER, along with a most positive onset potential of +0.96 V and the largest diffusion-limited current density of 4.64 mA cm^{-2} at 1600 rpm for ORR, as well as an overpotential of 28 mV at the current density of 10 mA cm^{-2} for HER. Both the ORR and HER performance are superior than commercial Pd/C. Furthermore, Mo_2C–Pd-9% exhibited markedly higher long-term durability toward both ORR and HER than Pd/C.

Experimental section

Chemicals

Ammonium molybdate ($(NH_4)_6Mo_7O_{24}\cdot 4H_2O$, ≥99.0% purchased from Damao Chemical Reagent, Tianjin, China), nitric acid (HNO_3, 65%–68%, purchased from Energy Chemicals, Shanghai, China), 3-hydroxytyramine hydrochloride (98%, purchased from Energy Chemicals, Shanghai, China), absolute ethanol (≥99.7%, purchased from Jinhuada Chemical Reagent, Guangzhou, China), ammonia solution (25%–28%, Cai Yunfei Chemical Industry), sodium tetrachloropalladate (II) (Na_2PdCl_4, 99.95%, purchased from Energy Chemicals, Shanghai, China). L-Ascorbic acid (AA, 98%, purchased from Energy Chemicals, Shanghai, China). All chemicals were used as received without purification. Deionized water was supplied by a Barnstead Nanopure Water System with a resistivity of 18.3 MΩ cm^{-1}.

Synthesis of MoO_3 nanorods

The MoO_3 nanorods were prepared by following a previously reported protocol [31]. In a typical reaction, 2.1 g of $(NH_4)_6Mo_7O_{24}\cdot 4H_2O$ was dissolved in 60 mL of mixed solvents of deionized water and HNO_3 (v: v = 5: 1). The mixed solution was then transferred into a Teflon-lined stainless steel autoclave (100 mL capacity) and heated at 200 °C for about 20 h. After cooling down, the product was collected by centrifugation and washed with deionized water and absolute ethanol for 3–5 times prior to drying at 70 °C overnight. The XRD patterns of the as-prepared MoO_3 nanorods can be found in Figure S1a, which agrees well with the previous reported results [28].

Synthesis of hierarchical β-Mo_2C nanotubes

The hierarchical β-Mo_2C nanotubes were prepared by following a previously documented synthetic method [28]. Firstly, 150 mg of the as-prepared MoO_3 nanorods were added into 30 mL of deionized water in a 250 mL glass beaker. After ultrasonic dispersion for 15 min, 300 mg of $(NH_4)_6Mo_7O_{24}\cdot 4H_2O$ and 75 mg of 3-hydroxytyramine hydrochloride were gradually dissolved into the above solution, and the milky solution turned into orange-red suspension. Then, 60 mL of absolute ethanol was added into the above solution rapidly. After stirring for 5 min, 450 μL of 28–30% $NH_3\cdot H_2O$ was injected into the above solution quickly, and the mixture was kept stirring for 120 min. Subsequently, the orange-red precipitate was obtained by suction filtration and washed with absolute ethanol for several times, followed by vacuum drying at room temperature for 12 h. Such orange-red solid was Mo-

polydopamine hybrids, and the XRD patterns (Figure S1b) were in good consistence with the reported results [28].

To obtain pure β-Mo_2C phase, the Mo-polydopamine hybrids were transferred to a quartz boat and annealed at 750 °C under an argon atmosphere for 16 h with a temperature ramp rate of 5 °C min^{-1}. Finally, the hierarchical β-Mo_2C nanotubes were obtained.

Fabrication of Pd nanoparticles grown on β-Mo_2C nanotubes

For all the samples, the amount of hierarchical β-Mo_2C nanotubes were kept as 20 mg, while the β-Mo_2C-to-Pd mass ratios were set as 100: 3, 100: 6, 100: 9, and 100: 12. The corresponding sample name was denoted as Mo_2C–Pd-3%, Mo_2C–Pd-6%, Mo_2C–Pd-9%, and Mo_2C–Pd-12%, respectively. The Mo_2C–Pd-9% sample was prepared as follows: Briefly, 20 mg of the as-prepared hierarchical β-Mo_2C nanotubes were added into 20 mL of deionized water in a 100 mL of round-bottom flask. After ultrasonic dispersion for 30 min, the round-bottom flask was transferred into an oil bath, and heated to 80 °C under magnetic stirring. Then 464.69 μL Na_2PdCl_4 (40 mM) aqueous solution was added into the flask. After stirring for a few mins, 464.69 μL freshly prepared AA (120 mM) aqueous solution was added to the above solution (the molar ratio of Na_2PdCl_4-to-AA equaling 3: 1) under vigorous stirring. Then the mixed solution was kept stirring for 24 h at 80 °C. After that, the product was collected by centrifugation and washed with deionized water and absolute ethanol for several times followed by vacuum drying at room temperature for 12 h. The other samples were synthesized in a similar manner by changing the volume of Na_2PdCl_4 and AA solutions correspondingly.

Characterization

The crystal structure of the samples was measured by X-ray diffraction (XRD) using a Bruker D8 diffractometer with Cu K_α radiation (λ = 0.1541 nm). The composition and valence state of the nanocomposites were analyzed by X-ray photoelectron spectroscopy (XPS) with an Escalab 250 photoelectron spectrometer (Thermo Fisher Scientific, USA). Scanning electronic microscopic (SEM) images were collected with a field emission scanning electron microscope (FESEM, Merlin). High-resolution transmission electron microscopic (HR-TEM) measurements were conducted with a transmission electron microscope (JEOL TEM-2010).

Electrochemical measurements

The ORR measurements were conducted on a CHI 750E electrochemical workstation (CH Instruments Inc.) in a 0.1 M KOH aqueous solution at room temperature with a conventional three-electrode system. A glassy carbon electrode (GCE, diameter 5 mm, Pine Instrument Inc., RRDE collection efficiency is 37%) that was coated with the catalysts prepared above was used as the working electrode, while a Pt plate and a Ag/AgCl wire with saturated KCl (3.0 M) were employed as the counter electrode and reference electrode, respectively. To prepare the working electrode, the GCE was first polished with 0.3 and 0.05 mm alumina slurries and rinsed extensively with water. Catalyst inks were prepared as follows: 2 mg of the catalysts prepared above was dispersed in 1.0 mL ethanol, and the above dispersion was sonicated for 30 min forming a homogeneous catalyst ink. A calculated amount of catalyst ethanol solution (10 μL) was then dropcast onto the GCE with the loading controlled at 20 μg after cleaned by polishing with aqueous slurries of 0.2 μm alumina powders on a polishing microcloth, and dried at room temperature. For commercial Pd/C (20 wt %), 2 mg Pd/C was well-dispersed in 1.0 mL ethanol and 10 μL of the ink was cast onto the glassy carbon disk electrode and dried at ambient temperature. Subsequently, 10 μL diluted Nafion solution (20 μL Nafion in 1 mL ethanol) was dropped on the dried samples and Pd/C catalyst. Cyclic voltammetric (CV) curves and linear sweep voltammograms (LSV) with various rotation rates from 400 to 2025 rpm were acquired at a scan rate of 10 mV s^{-1} in oxygen-saturated 0.1 M KOH solution. The stability of the catalysts was tested by chronoamperometric measurements at 0.45 V with a rotation rate of 900 rpm, and accelerated durability tests (ADT) from 0.6 V to 1.0 V at 50 mV s^{-1} were conducted in O_2-saturated 0.1 M KOH solution with a rotation rate of 1600 rpm before and after 3, 000 cycles of potential scans.

The HER measurements were performed on a CHI 750E electrochemical workstation (CH Instruments Inc.) in 0.5 M H_2SO_4 aqueous solution with a scan rate of 10 mV s^{-1} at ambient temperature. In 0.5 M H_2SO_4 aqueous solution, a glassy carbon electrode (geometrical area of 0.07 cm^2) and a graphite rod was employed as the working electrode and the counter electrode, respectively, while a saturated calomel electrode (SCE) was used as reference electrode in 0.5 M H_2SO_4. 1.25 times amount of sample and Pd/C catalysts used in ORR test was cast onto the working electrode in HER. The durability of the Mo_2C–Pd-9% catalysts was assessed by accelerated linear potential sweeps conducted repeatedly on the electrode at a scan rate of 100 mV s^{-1}.

In all electrochemical tests, the potential was referenced to a reversible hydrogen electrode (RHE): $E_{(RHE)} = E_{(Ag/AgCl)} + (0.197 + 0.0591^{*}pH)$ V, $E_{(RHE)} = E_{(SCE)} + (0.24 + 0.0591^{*}pH)$ V.

Results and discussion

TEM image analysis

The morphology of the as-obtained samples was firstly observed by transmission electron microscopy (TEM). From the typical TEM image of β-Mo_2C shown in Fig. 1a, a well-defined tube can be noted. The representative TEM image of the Mo_2C–Pd-9% sample can be found in Fig. 1b and c, and one can see that, spherical particles were uniformly dispersed on the surface of the tube. Representative TEM image of the other samples in the series including Mo_2C–Pd-3%, Mo_2C–Pd-6% and Mo_2C–Pd-12% can be found in Figure S2, and similar features can be easily identified. One may notice that, with relatively lower Pd loadings (3%, 6%, and 9%), the particles possessed a sphere-like shape, however, when the Pd loading reached 12%, heavy agglomeration occurred and bulky materials formed. The typical high-resolution (HR) TEM image of the Mo_2C–Pd-9% sample is presented in Fig. 1d, and from the inset amplified graph, crystalline and well-defined lattice

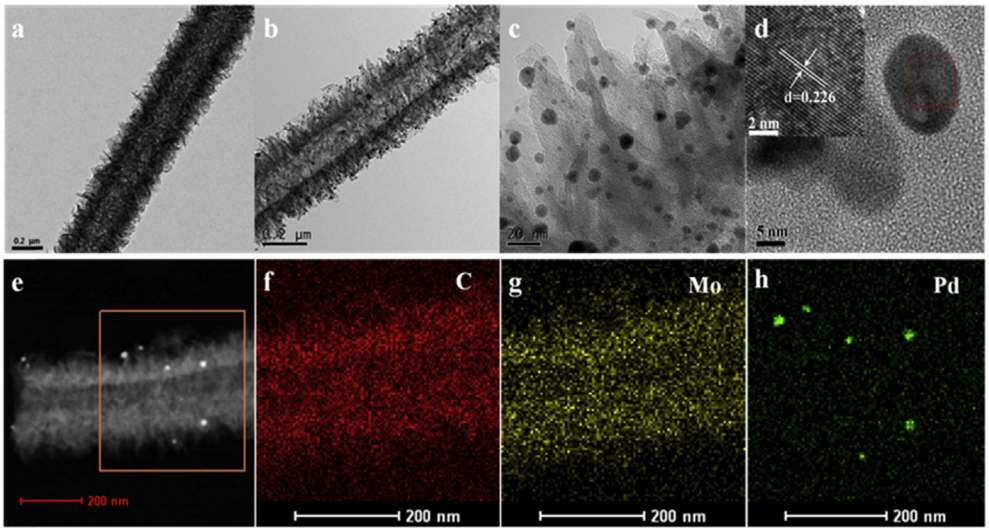

Fig. 1 – Representative TEM image of β-Mo_2C (a), and the Mo_2C–Pd-9% nanotubes (b), (c). (d) HR-TEM image of the hierarchical Mo_2C–Pd-9% nanotubes. (e) Black field-TEM image of the Mo_2C–Pd-9% sample, and EDS elemental mapping of (f) C, (g) Mo, and (h) Pd in the nanotubes.

fringes can be easily recognized. The interplanar spacing is estimated as 0.226 nm, which can be attributed to the (111) crystal plane of the palladium nanoparticles [32]. Fig. 1e shows the black-field TEM image of the Mo_2C–Pd-9% sample, and EDS mapping of the C, Mo and Pd elements can be found in Fig. 1f–1h. It can be noted that, all the elements are uniformly distributed with only a few larger Pd chunks formed, probably caused by the aggregation of small Pd nanoparticles. Furthermore, the atomic ratio of all the elements analyzed from the energy dispersive X-ray spectroscopy for the series of samples can be found in Figure S3. One may notice that, the actual atomic weight percentage for Mo_2C–Pd-9% is 7.78%, slightly lower than the initial loading value, and similar case occurred on the other samples in the series as well.

XRD and XPS measurements

Wide angle X-ray diffraction (XRD) measurements were then conducted to further probe the crystal structures of the series samples. As presented in Fig. 2a, β-Mo_2C exhibits several evident peaks at 34.6, 37.9, 39.6, 61.9, and 74.7°, which are ascribed to (100), (002), (101), (110), and (112) planes, respectively, while peaks observed at 39.9, 46.6, 67.9, 81.9, and 86.3° can be assigned to the (111), (200), (220), (311), and (222) crystal planes of Pd (JCPDS no. 01-087-0643). For all the Mo_2C–Pd samples, features from both Mo_2C and Pd are observed, indicating they were well integrated. In addition, with the increasing of Pd contents, the diffraction peaks from Pd gradually intensified. Subsequently, XPS measurements were conducted to elucidate elemental composition and corresponding valence states of the series samples. The survey scan spectra presented in Figure S4 confirmed the presence of C, O, Pd and Mo. Fig. 2b presents the high-resolution XPS spectra of the Mo3d electrons, and two peaks at ~232.7 eV and ~235.7 eV can be ascribed to the $3d_{5/2}$ and $3d_{3/2}$ electrons, respectively. It can be noted that, the peak from the $3d_{3/2}$ electrons can be further de-convoluted into four peaks, which correspond to four oxidation peaks of Mo^0, Mo^{3+}, Mo^{4+} and Mo^{6+}, respectively. The results agree well with previous reports [17,33]. In addition, the high-resolution XPS spectra from the Pd 3d electron is illustrated in Fig. 3c, which can de-convoluted into two doublets [34,35]. The pair at lower energies (335.8 eV and 341.00 eV) can be attributed to metallic Pd, whereas those at somewhat higher energies (337.5 eV and 342.6 eV) are consistent with to Pd(II) species [19,36,37]. It indicates the formation of a substantial amount of palladium oxide in the sample.

The ORR performance of the series of samples and commercial Pd/C

The series of samples were then subjected to electrocatalytic tests toward ORR by cyclic voltammetric (CV) and linear sweep voltammetric (LSV) measurements. The electrocatalytic activity of all the samples are compiled in Table S1. As depicted in Figure S5, in O_2-saturated 0.1 M KOH, a cathodic peak ascribed to oxygen reduction appeared from 0.70 V to 0.90 V in CV curves for the series of sample and commercial Pd/C, indicating effective catalytic activity. Notably, Mo_2C exhibited negligible ORR activity. Interestingly, the catalytic activity varied dramatically with the variation of Pd loading. With the increasing of Pd loading, the cathodic peak potential first increased then decreased, while Mo_2C–Pd-9% possessed the highest cathodic peak potential value. Such ORR activity change trend was further verified by RRDE measurement. From the LSV curves in Fig. 3a, the onset potential and diffusion-limited current of the series sample and Mo_2C can be estimated. Again, Mo_2C had negligible activity. The onset potential is estimated as 0.91, 0.93, 0.96, and 0.93 V for the sample of Mo_2C–Pd-3%, Mo_2C–Pd-6%, Mo_2C–Pd-9%, and Mo_2C–Pd-12%, while the diffusion limited current density is −3.83, −4.53, −4.64, and −4.36 mA cm^{-2} for the sample of Mo_2C–Pd-3%, Mo_2C–Pd-6%, Mo_2C–Pd-9%, and Mo_2C–Pd-12%, respectively. Note that, both values first increased then

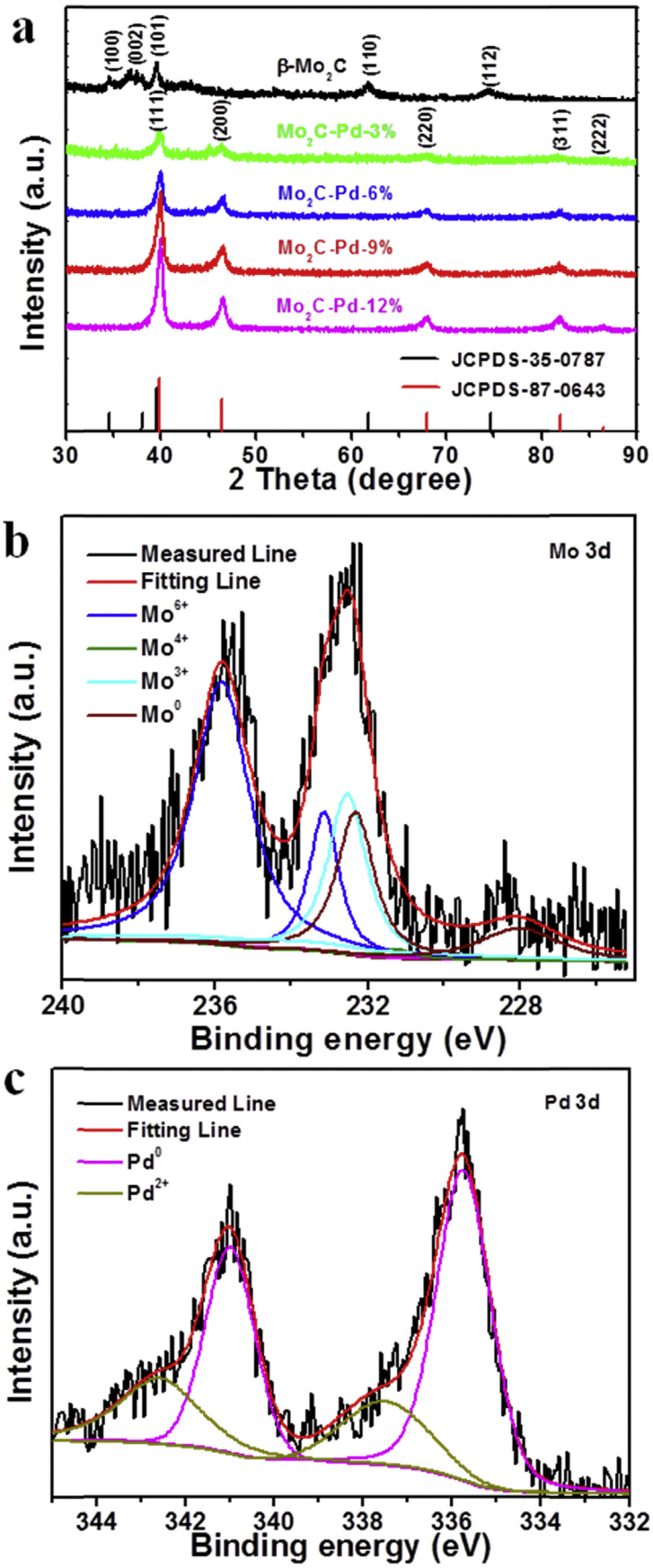

Fig. 2 – (a) XRD patterns of the Mo_2C, Mo_2C–Pd-3%, Mo_2C–Pd-6%, Mo_2C–Pd-9%, and Mo_2C–Pd-12% samples, and XPS core-level spectra of (b) Mo 3d and (c) Pd 3d electrons for the Mo_2C–Pd-9% sample.

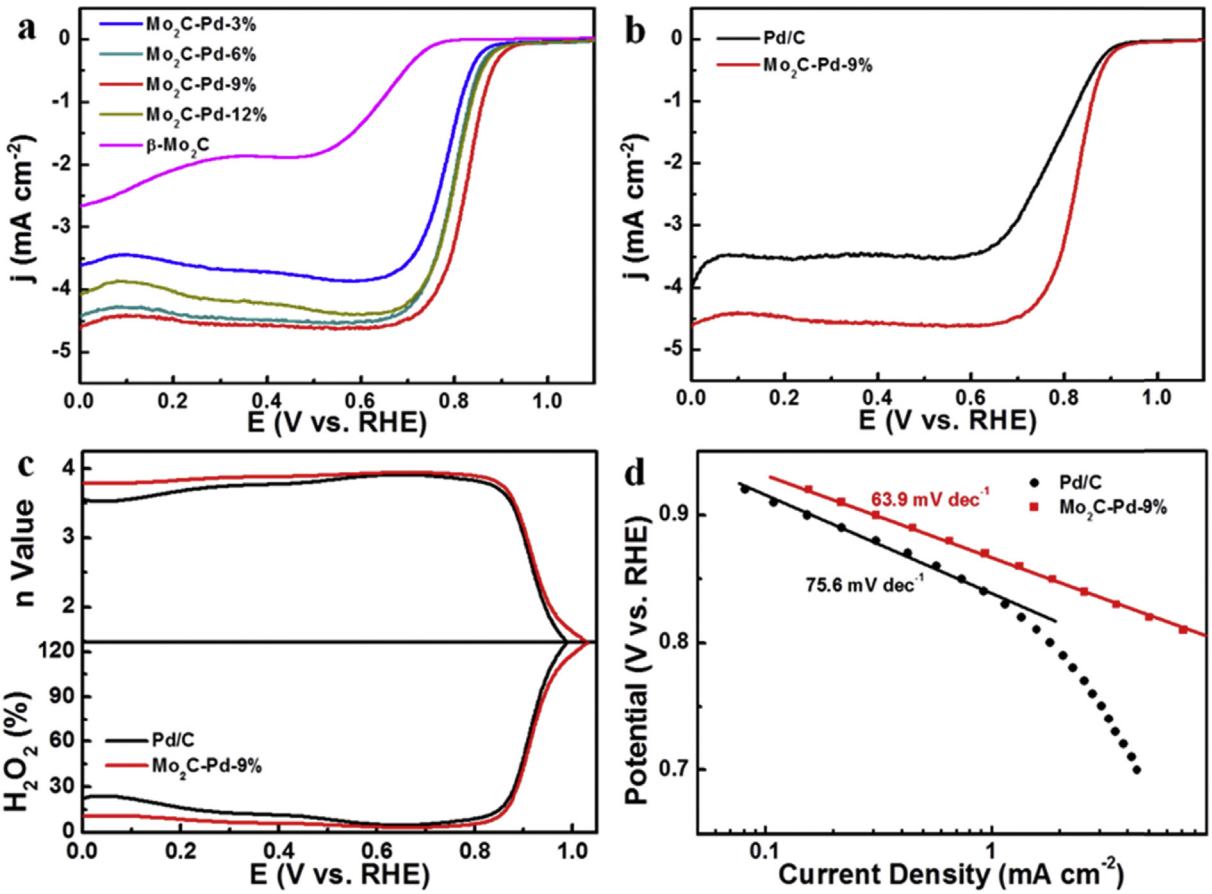

Fig. 3 – (a) RRDE voltammograms measurements of the β-Mo_2C, Mo_2C–Pd-3%, Mo_2C–Pd-6%, Mo_2C–Pd-9%, and Mo_2C–Pd-12% in O_2-saturated 0.1 M KOH solution. Potential scan rate is 10 mV s^{-1} and the rotation rate is 1600 rpm. RRDE voltammograms (b), plots of H_2O_2 yield and electron transfer numbers (c) and the corresponding Tafel plots (d) of the Mo_2C–Pd-9% sample and Pd/C catalyst.

decreased with the increasing of Pd loading while the sample of Mo_2C–Pd-9% possessed the best ORR performance, manifested by the most positive onset potential and the largest diffusion-limited current density.

The ORR activity of the Mo_2C–Pd-9% was further examined and compared with commercial Pd/C catalyst. As illustrated in Fig. 3b, Mo_2C–Pd-9% exhibited slightly more positive onset potential and much larger diffusion-limited current density than Pd/C. Moreover, the number of electron transfer (n) and yield of hydrogen peroxide (H_2O_2%) at different potentials can be calculated through the following equations [38,39].

$$n = \frac{4I_D}{I_D + \frac{I_R}{N}} \quad (1)$$

$$H_2O_2\% = \frac{\frac{200I_R}{N}}{\frac{I_R}{N} + I_D} \quad (2)$$

where I_R is the ring current, I_D is the disk current and N is the current collection efficiency of the RRDE (0.37). The calculated results are presented in Fig. 3c. The number of electron transfer of Mo_2C–Pd-9% was 3.83–3.94 in the potential range of 0.2–0.8 V, slightly higher than that of commercial Pd/C (3.67–3.91), indicating that the reaction proceeded predominantly with the $4e^-$ pathway in 0.1 M KOH solution for both catalysts [19,36,40]. Correspondingly, Mo_2C–Pd-9% exhibits slightly lower value of H_2O_2 yield (3.1%–8.4%) than that of commercial Pd/C (4.7%–16.5%) in the potential range of 0.2–0.8 V. The higher electron transfer number and lower H_2O_2 yield indicate that Mo_2C–Pd-9% possessed superior catalytic activity toward ORR than commercial Pd/C.

Subsequently, the reaction kinetics toward ORR for Mo_2C–Pd-9% and commercial Pd/C can be analyzed by the extrapolated Tafel plots. As presented in Fig. 3d, the Tafel slope was calculated as 63.9 mV dec^{-1} and 76.5 mV dec^{-1} for the sample of Mo_2C–Pd-9% and commercial Pd/C, respectively. Note that, such values are in good accordance with the typical values obtained with structured palladium nanoparticles or supported palladium nanoarchitectures in ORR [19,36,40,41]. Furthermore, the much lower Tafel slope than commercial Pd/C further attest that, Mo_2C–Pd-9% possessed superior activity and faster reaction kinetics than commercial Pd/C in the electrocatalytic oxygen reduction process.

The long-term durability of Mo_2C–Pd-9% compared with Pd/C for ORR

The long-term stability of the Mo_2C–Pd-9% sample for ORR was then tested and compared with commercial Pd/C [40].

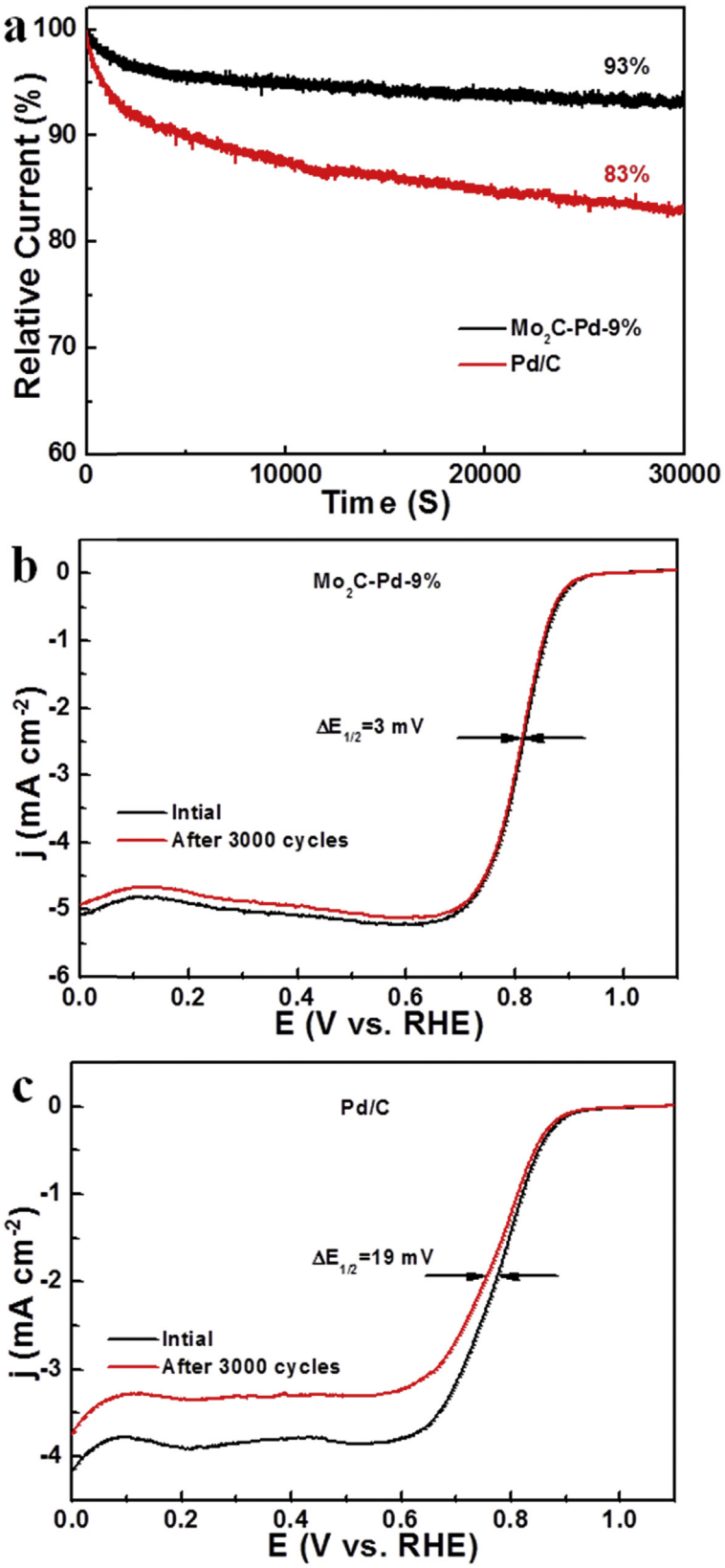

Fig. 4 – (a) Chronoamperometric curves (a) of the Mo_2C–Pd-9% sample and Pd/C catalyst at + 0.45 V for 30, 000 s. The accelerated durability tests (ADT) of the Mo_2C–Pd-9% sample (b) and Pd/C catalyst (c) before and after 3000 cycles between 0.6 and 1.0 V at a scan rate of 50 mV s^{-1}. All measurements were conducted in an O_2-saturated 0.1 M KOH solution.

Fig. 4a presents the chronoamperometric responses at 0.45 V in O_2-saturated 0.1 M KOH solution. It can be observed that, the initial current density dropped to 83% after continuous operation of about ~8 h for Pd/C, while in sharp contrast, the Mo_2C–Pd-9% sample can retain 93%, indicating a more robust catalytic durability. Furthermore, accelerated durability test (ADT) was conducted to evaluate its long-term stability by cycling the catalyst over the potential range from 0.6 V to 1.0 V at 50 mV s^{-1} in 0.1 M KOH [19]. As shown in Fig. 4b and c, the half-wave potential shifted negatively about ~19 mV after 3, 000 cycles, while only ~3 mV negative shift was observed for Mo_2C–Pd-9%, further confirming the much durable long-term stability than that of commercial Pd/C.

The HER activity tests compared with Pd/C

In addition to ORR, the electrocatalytic activities toward HER of the series of the samples were also examined in 0.5 M H_2SO_4 [42,43], and the results are summarized in Table S1. As shown in the LSV curves in Fig. 5a, the series of samples exhibited effective HER activity with the variation of Pd loading, and the HER activity first increased then decreased with the increasing of Pd loading (Table S1). Such change trend agreed well with the above ORR tests. The Mo_2C–Pd-9% sample exhibited the best HER activity. One may notice that, for the samples of Mo_2C–Pd-6%, Mo_2C–Pd-9%, and Mo_2C–Pd-12%, there is a hydrogen adsorption peak located at between −0.05 V and 0.10 V. Such hydrogen adsorption behaviors from Pd nanomaterials have been well recorded in several previous reports [44–46]. The higher amount of Pd in the three samples led to the increase of electrocatalytically active sites from Pd surface, which resulted in the appearance of such phenomenon [18]. The electrocatalytic activity of the Mo_2C–Pd-9% sample was then compared with commercial Pd/C. As depicted in Fig. 5b, to afford a current density of 10 mA cm^{-2}, the required overpotential was 28 mV and 45 mV for the sample of Mo_2C–Pd-9% and Pd/C, respectively, implying that the HER activity of Mo_2C–Pd-9% is superior than Pd/C. The corresponding Tafel plots were then extrapolated, and the Tafel slope was calculated as 51.0 mV dec^{-1} and 70.1 mV dec^{-1} for Mo_2C–Pd-9% and Pd/C, respectively. The much lower Tafel slope from the Mo_2C–Pd-9% suggests that a faster reaction kinetics was adopted during the electrocatalytic process. Finally, the long-term stability of the Mo_2C–Pd-9% sample was assessed and compared with Pd/C in 0.5 M H_2SO_4 toward HER. After continuous operation of about 8 h, the initial current density retained 72.4% for Pd/C, while 90.6% of the starting current density preserved for Mo_2C–Pd-9%, suggesting a markedly higher long-term stability.

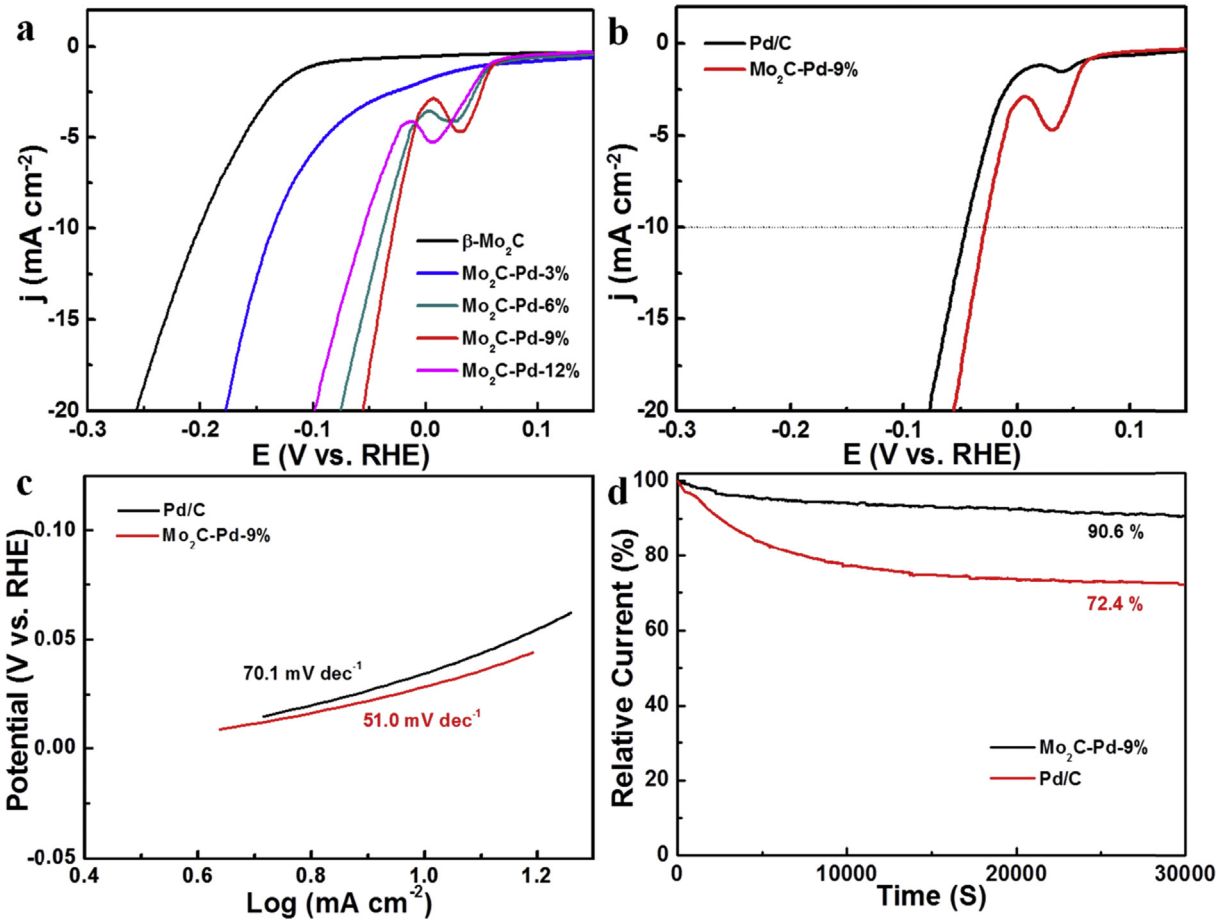

Fig. 5 – HER polarization curves of the β-Mo_2C, Mo_2C–Pd-3%, Mo_2C–Pd-6%, Mo_2C–Pd-9%, Mo_2C–Pd-12% (a), and the β-Mo_2C–Pd-9% sample and Pd/C catalyst (b) in 0.5 M H_2SO_4 with a scan rate of 10 mV s^{-1}. (c) HER stability tests of Mo_2C–Pd-9% and Pd/C in 0.5 M H_2SO_4 for 30, 000 s. (d) The corresponding Tafel plots of the Mo_2C–Pd-9% sample and Pd/C catalyst.

Conclusions

In conclusion, we have developed a facile approach to prepare Pd nanoparticles grown on Mo_2C nanotubes as dual functional electrocatalysts for both ORR and HER. A series of samples with different Pd loadings were fabricated, while the morphology and the structural features were well examined by TEM, XRD, XPS and other techniques. Interestingly, both the ORR activity and HER activity first increased then decreased with the increasing of Pd loading, and the sample of Mo_2C–Pd-9% exhibited the best performance among the series, superior than commercial Pd/C in both ORR and HER tests. Furthermore, it also exhibited markedly higher long-term stability than Pd/C for both electrocatalytic reactions. The results may shed light on rational design of novel bi-functional electrocatalysts in the renewable energy field.

Acknowledgements

This work was supported by the National Natural Science Foundation of China (No. 21501059 from Z. H. T and No. 51306040 from C. H. W). Z. H. T also acknowledges financial support from Science and Technology Program of Guangdong Province (No. 2017A050506014), Project of Public Interest Research and Capacity Building of Guangdong Province (2015A010105009), Guangdong Innovative and Entrepreneurial Research Team Program (No. 2014ZT05N200), Guangdong Natural Science Funds for Distinguished Young Scholars (No. 2015A030306006).

Appendix A. Supplementary data

Supplementary data related to this article can be found at https://doi.org/10.1016/j.ijhydene.2018.01.107.

REFERENCES

[1] Li Y, Dai H. Recent advances in zinc-air batteries. Chem Soc Rev 2014;43:5257–75.
[2] Wang Y-J, Zhao N, Fang B, Li H, Bi XT, Wang H. Carbon-supported Pt-based alloy electrocatalysts for the oxygen reduction reaction in polymer electrolyte membrane fuel cells: particle size, shape, and composition manipulation and their impact to activity. Chem Rev 2015;115:3433–67.
[3] Walter MG, Warren EL, McKone JR, Boettcher SW, Mi Q, Santori EA, et al. Solar water splitting cells. Chem Rev 2010;110:6446–73.
[4] Kraytsberg A, Ein-Eli Y. Review of advanced materials for proton exchange membrane fuel cells. Energy Fuels 2014;28:7303–30.
[5] Liu M, Zhang R, Chen W. Graphene-supported nanoelectrocatalysts for fuel cells: synthesis, properties, and applications. Chem Rev 2014;114:5117–60.
[6] Wang J, Xu F, Jin H, Chen Y, Wang Y. Non-noble metal-based carbon composites in hydrogen evolution reaction: fundamentals to applications. Adv Mater 2017;29:1605838.
[7] Zhang H, Osgood H, Xie X, Shao Y, Wu G. Engineering nanostructures of PGM-free oxygen-reduction catalysts using metal-organic frameworks. Nano Energy 2017;31:331–50.
[8] Othman R, Dicks AL, Zhu Z. Non precious metal catalysts for the PEM fuel cell cathode. Int J Hydrogen Energy 2012;37:357–72.
[9] Wang W, Lei B, Guo S. Engineering multimetallic nanocrystals for highly efficient oxygen reduction catalysts. Adv Energy Mater 2016;6:1600236.
[10] Strmcnik D, Lopes PP, Genorio B, Stamenkovic VR, Markovic NM. Design principles for hydrogen evolution reaction catalyst materials. Nano Energy 2016;29:29–36.
[11] Eftekhari A. Electrocatalysts for hydrogen evolution reaction. Int J Hydrogen Energy 2017;42:11053–77.
[12] Lu Y, Jiang Y, Gao X, Wang X, Chen W. Strongly coupled Pd nanotetrahedron/tungsten oxide nanosheet hybrids with enhanced catalytic activity and stability as oxygen reduction electrocatalysts. J Am Chem Soc 2014;136:11687–97.
[13] Niu W, Li L, Liu X, Wang N, Liu J, Zhou W, et al. Mesoporous N-Doped carbons prepared with thermally removable nanoparticle templates: an efficient electrocatalyst for oxygen reduction reaction. J Am Chem Soc 2015;137:5555–62.
[14] Wu G, Wang J, Ding W, Nie Y, Li L, Qi X, et al. A strategy to promote the electrocatalytic activity of spinels for oxygen reduction by structure reversal. Angew Chem Int Ed 2016;vol. 55:1340–4.
[15] Liu K, Song Y, Chen S. Oxygen reduction catalyzed by nanocomposites based on graphene quantum dots-supported copper nanoparticles. Int J Hydrogen Energy 2016;41:1559–67.
[16] Ha D-H, Han B, Risch M, Giordano L, Yao KPC, Karayaylali P, et al. Activity and stability of cobalt phosphides for hydrogen evolution upon water splitting. Nano Energy 2016;29:37–45.
[17] Li J-S, Wang Y, Liu C-H, Li S-L, Wang Y-G, Dong L-Z, et al. Coupled molybdenum carbide and reduced graphene oxide electrocatalysts for efficient hydrogen evolution. Nat Commun 2016;7:11204.
[18] Chen A, Ostrom C. Palladium-based nanomaterials: synthesis and electrochemical applications. Chem Rev 2015;115:11999–2044.
[19] Yan W, Tang Z, Li L, Wang L, Yang H, Wang Q, et al. Ultrasmall palladium nanoclusters encapsulated in porous carbon nanosheets for oxygen electroreduction in alkaline media. ChemElectroChem 2017;4:1349–55.
[20] Zhang L, Chang Q, Chen H, Shao M. Recent advances in palladium-based electrocatalysts for fuel cell reactions and hydrogen evolution reaction. Nano Energy 2016;29:198–219.
[21] Erikson H, Sarapuu A, Solla-Gullón J, Tammeveski K. Recent progress in oxygen reduction electrocatalysis on Pd-based catalysts. J Electroanal Chem 2016;780:327–36.
[22] Begum H, Ahmed MS, Cho S, Jeon S. Freestanding palladium nanonetworks electrocatalyst for oxygen reduction reaction in fuel cells. Int J Hydrogen Energy 2018;43:229–38.
[23] Zhou W, Li M, Ding OL, Chan SH, Zhang L, Xue Y. Pd particle size effects on oxygen electrochemical reduction. Int J Hydrogen Energy 2014;39:6433–42.
[24] Shao M, Odell J, Humbert M, Yu T, Xia Y. Electrocatalysis on shape-controlled palladium nanocrystals: oxygen reduction reaction and formic acid oxidation. J Phys Chem C 2013;117:4172–80.
[25] Liao H, Wei C, Wang J, Fisher A, Sritharan T, Feng Z, et al. A multisite strategy for enhancing the hydrogen evolution reaction on a Nano-Pd surface in alkaline media. Adv Energy Mater 2017;7:1701129.
[26] Liu S, Mu X, Duan H, Chen C, Zhang H. Pd nanoparticle assemblies as efficient catalysts for the hydrogen evolution

and oxygen reduction reactions. Eur J Inorg Chem 2017;2017:535–9.
[27] Sharma S, Pollet BG. Support materials for PEMFC and DMFC electrocatalysts—a review. J Power Source 2012;208:96–119.
[28] Ma F-X, Wu HB, Xia BY, Xu C-Y, Lou XW. Hierarchical β-Mo2C nanotubes organized by ultrathin nanosheets as a highly efficient electrocatalyst for hydrogen production. Angew Chem Int Ed 2015;vol. 54:15395–9.
[29] Wu HB, Xia BY, Yu L, Yu X-Y, Lou XW. Porous molybdenum carbide nano-octahedrons synthesized via confined carburization in metal-organic frameworks for efficient hydrogen production. Nat Commun 2015;6:6512.
[30] Meyer S, Nikiforov AV, Petrushina IM, Köhler K, Christensen E, Jensen JO, et al. Transition metal carbides (WC, Mo_2C, TaC, NbC) as potential electrocatalysts for the hydrogen evolution reaction (HER) at medium temperatures. Int J Hydrogen Energy 2015;40:2905–11.
[31] Chen JS, Cheah YL, Madhavi S, Lou XW. Fast synthesis of α-MoO3 nanorods with controlled aspect ratios and their enhanced lithium storage capabilities. J Phys Chem C 2010;114:8675–8.
[32] Zheng J-N, Li S-S, Ma X, Chen F-Y, Wang A-J, Chen J-R, et al. Green synthesis of core–shell gold–palladium@palladium nanocrystals dispersed on graphene with enhanced catalytic activity toward oxygen reduction and methanol oxidation in alkaline media. J Power Sources 2014;262:270–8.
[33] Cheng Z, Gao J, Fu Q, Li C, Wang X, Xiao Y, et al. Interconnected molybdenum carbide-based nanoribbons for highly efficient and ultrastable hydrogen evolution. ACS Appl Mater Interfaces 2017;9:24608–15.
[34] Wagner CD, Riggs WM, Davis LE, Moudler JF, Muilenberg GE. Handbook of x-ray photoelectron spectroscopy: a reference book of standard data for use in x-ray photoelectron spectroscopy. MN: Perkin-Elmer Corp: Edern Prairie; 1979. 1979.
[35] Moulder JF, Stickle WF, Sobol PE, Bomben KD. Handbooks of x-ray photoelectron spectroscopy. MN, USA: published by Perkin-Elmer Corp; 1992.
[36] Deming CP, Mercado R, Lu JE, Gadiraju V, Khan M, Chen S. Oxygen electroreduction catalyzed by palladium nanoparticles supported on nitrogen-doped graphene quantum dots: impacts of nitrogen dopants. ACS Sustain Chem Eng 2016;4:6580–9.
[37] Li D, Tang Z, Chen S, Tian Y, Wang X. Peptide-FlgA3-Based gold palladium bimetallic nanoparticles that catalyze the oxygen reduction reaction in alkaline solution. ChemCatChem 2017;9:2980–7.
[38] Yan W, Tang Z, Wang L, Wang Q, Yang H, Chen S. PdAu alloyed clusters supported by carbon nanosheets as efficient electrocatalysts for oxygen reduction. Int J Hydrogen Energy 2017;42:218–27.
[39] Wang Q, Yang H, Zhou Z, Wang L, Yan W, Wu W, et al. Peptide A4 based AuAg alloyed nanoparticle networks for electrocatalytic reduction of oxygen. Int J Hydrogen Energy 2017;42:11295–303.
[40] Yang H, Tang Z, Yan W, Wang L, Wang Q, Zhang Y, et al. Peptide capped Pd nanoparticles for oxygen electroreduction: strong surface effects. J Alloys Compd 2017;702:146–52.
[41] Deming CP, Mercado R, Gadiraju V, Sweeney SW, Khan M, Chen S. Graphene quantum dots-supported palladium nanoparticles for efficient electrocatalytic reduction of oxygen in alkaline media. ACS Sustain Chem Eng 2015;3:3315–23.
[42] Kuang M, Wang Q, Han P, Zheng G. Cu, Co-Embedded N-Enriched mesoporous carbon for efficient oxygen reduction and hydrogen evolution reactions. Adv Energy Mater 2017;7:1700193.
[43] Lin X-X, Zhang X-F, Wang A-J, Fang K-M, Yuan J, Feng J-J. Simple one-pot aqueous synthesis of AuPd alloy nanocrystals/reduced graphene oxide as highly efficient and stable electrocatalyst for oxygen reduction and hydrogen evolution reactions. J Colloid Interface Sci 2017;499:128–37.
[44] Łukaszewski M, Klimek K, Żurowski A, Kędra T, Czerwiński A. Kinetics and mechanism of hydrogen electrosorption in palladium-based alloys. Solid State Ionics 2011;190:18–24.
[45] Safavi A, Kazemi SH, Kazemi H. Electrocatalytic behaviors of silver–palladium nanoalloys modified carbon ionic liquid electrode towards hydrogen evolution reaction. Fuel 2014;118:156–62.
[46] Ghasemi S, Hosseini SR, Nabipour S, Asen P. Palladium nanoparticles supported on graphene as an efficient electrocatalyst for hydrogen evolution reaction. Int J Hydrogen Energy 2015;40:16184–91.